

First-principles study of the optical properties of $\text{Mg}_x\text{Ti}_{(1-x)}\text{H}_2$

M.J. van Setten¹, S. Er², G. Brocks², R.A. de Groot^{1,3}, and G.A. de Wijs¹

¹*Electronic Structure of Materials, Institute for Molecules and Materials,
Faculty of Science, Radboud University Nijmegen,
Toernooiveld 1, 6525 ED Nijmegen, The Netherlands*

²*Computational Materials Science, Faculty of Science and Technology and MESA+ Institute for Nanotechnology,
University of Twente, P.O. Box 217, 7500 AE Enschede, The Netherlands and*

³*Laboratory of Solid State Chemistry, Zernike Institute for Advanced Materials,
Rijksuniversiteit Groningen, Nijenborgh 4, 9747 AG Groningen, The Netherlands*

(Dated: April 2, 2008)

The optical and electronic properties of Mg-Ti hydrides are studied using first-principles density functional theory. Dielectric functions are calculated for $\text{Mg}_x\text{Ti}_{(1-x)}\text{H}_2$ with compositions $x = 0.5$, 0.75 , and 0.875 . The structure is that of fluorite TiH_2 where both Mg and Ti atoms reside at the Ti positions of the lattice. In order to assess the effect of randomness in the Mg and Ti occupations we consider both highly ordered structures, modeled with simple unit cells of minimal size, and models of random alloys. These are simulated by super cells containing up to 64 formula units ($Z = 64$). All compositions and structural models turn out metallic, hence the dielectric functions contain interband and intraband free electron contributions. The former are calculated in the independent particle random phase approximation. The latter are modeled based upon the intraband plasma frequencies, which are also calculated from first-principles. Only for the models of the random alloys we obtain a black state, i.e. low reflection and transmission in the energy range from 1 to 6 eV.

PACS numbers: 71.20.-b, 71.15.Nc, 61.72.Bb, 74.62.Dh

I. INTRODUCTION

Since the discovery of the switchable mirror YH_x by Huiberts *et al.*¹ in 1996 several other metal hydride systems that behave as switchable mirrors have been discovered.^{1,2,3,4,5,6} The metals are reflective, but after hydrogenation become semiconductors and hence in most cases become transparent. Especially when an alloy with high hydrogen mobility is used and when applied as thin films the optical switching can be fast, reversible and robust.⁷

Recently, meta-stable thin films composed of various ratios of magnesium and titanium have been shown to exhibit remarkable optical properties which could be especially useful for smart solar cell coatings and hydrogen sensor applications.^{6,8} In the dehydrogenated state the films are highly reflective. Upon hydrogenation they become black, i.e. have a low reflection and high absorption in the energy range of the solar spectrum. The structural and electronic characteristics of this black state are a topic of intensive research.^{9,10}

Obtaining structural data for these systems is difficult. Single crystals cannot be grown as the compounds are thermodynamically unstable. For a 7:1 ratio of magnesium to titanium Kyojima *et al.*, using a sample prepared at high pressure, could determine the crystal structure.¹¹ It is similar to the fluorite TiH_2 structure. Notten and co-workers (Refs. 12,13) and Borsa *et al.*^{6,9} have shown that for higher titanium content ($x < 0.8$) the structure is fluorite-like as well. At lower lower titanium concentrations a rutile ($\alpha\text{-MgH}_2$ like) structure is found. Interestingly, the kinetics of the hydrogen ab/desorption reactions are much faster in the fluorite structures than in the rutile structures.¹⁴ The equality of the molar volume

of TiH_2 and Mg has been used to explain the structural stability of the meta-stable “phases”.⁹ Calculations using density functional theory (DFT) find the same composition dependence of the relative stability of the rutile and fluorite structures.¹⁰

The origin of the “black state” is not understood. Its explanation is, of course, intimately related to the electronic structure of the hydride. In experiments, usually less than two hydrogen atoms per metal atom can be reversibly absorbed and desorbed.⁹ Electrochemically 1.7 hydrogen atoms per metal atom can be stored reversibly.¹⁴ Moreover, the crystal structure of Mg_7TiH_x as determined by Kyojima *et al.*¹¹ is estimated to contain 1.6 hydrogen atoms per metal atom. All this suggests that maximally two metal electrons per metal atom can be transferred to hydrogen.⁹ Hence the Ti atoms remain in an open-shell configuration with at least two d -electrons left. The above reasoning has been confirmed by DFT calculations on crystalline $\text{Mg}_x\text{Ti}_{(1-x)}\text{H}_2$ structures.¹⁰ The calculated densities of states show predominant hydrogen- s character below the Fermi level, which is typical for metal hydrides, and titanium- d states at the Fermi level. These are likely to form metallic bands, so one expects $\text{Mg}_x\text{Ti}_{1-x}\text{H}_2$ to be reflective instead of black. Moreover, experimental investigation of the electrical transport properties reveal high resistivity 1.32–1.9 m Ωcm , with a logarithmic, hence non-metallic, temperature dependence.⁹ In order to explain these results the formation of a so-called coherent crystal structure was proposed,⁹ wherein regions of insulating MgH_2 and metallic TiH_2 coexist.

In an effort to advance the understanding of the black state, in this paper we report a computational study of the optical and electronic properties of $\text{Mg}_x\text{Ti}_{(1-x)}\text{H}_2$ for

$x = 0.5, 0.75$ and 0.875 . We employ both simple (i.e. minimal) unit cells and large super cells of the same compositions. The latter model random alloys wherein the Mg and Ti are distributed over the lattice sites of a TiH_2 -like structure. Details of these models are presented in Ref. 10.

The dielectric functions consist of intra and interband contributions:

$$\varepsilon(\omega) = \varepsilon_{\text{inter}}(\omega) + \varepsilon_{\text{intra}}(\omega) . \quad (1)$$

These are calculated separately. For the interband contribution $\varepsilon_{\text{inter}}$ we use first-principles DFT in the independent particle random phase approximation. Since the materials in question are metals, the intraband dielectric part $\varepsilon_{\text{intra}}$ does not vanish. It is modeled from the plasma frequencies ω_p , which are calculated from first-principles as well.

In Sec. II the technical details of the calculations are summarized. Sec. III contains a concise description of the structural models used. Results on the dielectric functions are presented in Sec. IV. Finally, in the discussion section (Sec. V) results are compared with experiment.⁹

II. COMPUTATIONAL METHODS

First-principles DFT calculations were carried out with the Vienna *Ab initio* Simulation Package (VASP),^{15,16,17} using the projector augmented wave (PAW) method.^{18,19} A plane wave basis set was used and periodic boundary conditions applied. The kinetic energy cutoff on the Kohn-Sham states was 312.5 eV. For the exchange-correlation functional we used the generalized gradient approximation (GGA).²⁰ Non-linear core corrections were applied.²¹

The Brillouin zone integrations were performed using a Gaussian smearing method with a width of 0.1 eV.²² The \mathbf{k} -point meshes were even grids containing Γ so that the band extrema are typically included in the calculation of the dielectric functions. The convergence of the dielectric functions and intraband plasma frequencies with respect to the \mathbf{k} -point meshes was tested by increasing the number of \mathbf{k} -points for each system separately. A typical mesh spacing of about 0.01 \AA^{-1} was needed to obtain converged results.

The calculations of the complex interband dielectric functions, $\varepsilon_{\text{inter}}(\omega) = \varepsilon_{\text{inter}}^{(1)}(\omega) + i\varepsilon_{\text{inter}}^{(2)}(\omega)$, were performed in the random phase independent particle approximation, i.e. taking into account only direct transitions from occupied to unoccupied Kohn-Sham orbitals. Local field effects were neglected. The imaginary part of the macroscopic dielectric function, $\varepsilon_{\text{intra}}^{(2)}(\omega)$, than has the form:

$$\varepsilon_{\text{inter}}^{(2)}(\hat{\mathbf{q}}, \omega) = \frac{8\pi^2 e^2}{V} \lim_{|\mathbf{q}| \rightarrow 0} \frac{1}{|\mathbf{q}|^2} \times \sum_{\mathbf{k}, v, c} |\langle u_{c, \mathbf{k}+\mathbf{q}} | u_{v, \mathbf{k}} \rangle|^2 \delta(\epsilon_{c, \mathbf{k}+\mathbf{q}} - \epsilon_{v, \mathbf{k}} - \hbar\omega) \quad (2)$$

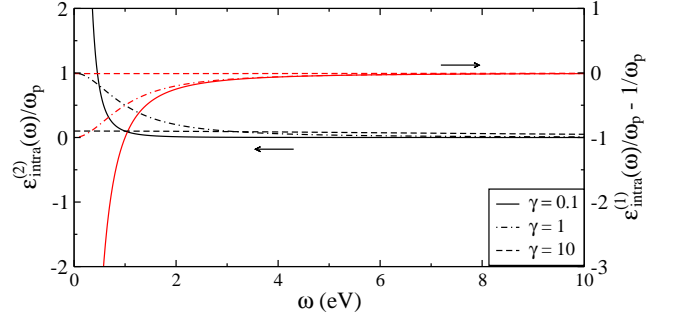


FIG. 1: (Color online) Dielectric functions of a free electron gas according to equation 3.

where $\hat{\mathbf{q}}$ denotes the direction of \mathbf{q} and $v, \mathbf{k} + \mathbf{q}$ and c, \mathbf{k} label single particle states that are occupied and unoccupied in the ground state, respectively. ϵ, u are the single particle energies and the translationally invariant parts of the wave functions. V is the volume of the unit cell. The real part, $\varepsilon_{\text{inter}}^{(1)}(\omega)$, is obtained via a Kramers-Kronig transform. Further details can be found in Ref. 23.

Most optical data on hydrides are obtained from micro- and nano-crystalline samples whose crystallites have a significant spread in orientation. Therefore the most relevant quantity is the directionally averaged dielectric function, i.e. $\varepsilon_{\text{inter}}^{(2)}(\omega)$ averaged over $\hat{\mathbf{q}}$.

The intraband dielectric function, $\varepsilon_{\text{intra}}(\omega) = \varepsilon_{\text{intra}}^{(1)}(\omega) + i\varepsilon_{\text{intra}}^{(2)}(\omega)$, is calculated from the free electron plasma frequency ω_p :

$$\varepsilon_{\text{intra}}^{(1)}(\omega) = 1 - \frac{\omega_p^2}{\omega^2 + \gamma^2} \quad (3)$$

$$\varepsilon_{\text{intra}}^{(2)}(\omega) = \frac{\gamma\omega_p^2}{\omega^3 + \omega\gamma^2} \quad (4)$$

where an inverse lifetime, $\gamma = 0.01 \text{ eV}$, is used. For $\gamma = 0$ the reflection would be perfect up to the plasma frequency and zero beyond. Finite values of γ decrease the reflection below ω_p and smoothen the reflection edge at ω_p . For metals γ values are in the order of 0.1 eV. By using a small value the influence of the interband part is emphasized. Calculating γ from first principles obviously goes beyond DFT. For three values of γ the free electron $\varepsilon_{\text{intra}}$ is plotted in Fig. 1.

The plasma frequency ω_p is calculated as an integral over the Fermi surface according to:

$$\omega_{p(\alpha\beta)}^2 = \frac{4\pi e^2}{V\hbar^2} \sum_{n, \mathbf{k}} 2g_{\mathbf{k}} \frac{\partial f(\epsilon_{n\mathbf{k}})}{\partial \epsilon} \left(\mathbf{e}_\alpha \frac{\partial \epsilon_{n\mathbf{k}}}{\partial \mathbf{k}} \right) \left(\mathbf{e}_\beta \frac{\partial \epsilon_{n\mathbf{k}}}{\partial \mathbf{k}} \right) \quad (5)$$

with $g_{\mathbf{k}}$ the weight factors, and $f(\epsilon_{n\mathbf{k}})$ the occupation function. Again we use directionally averaged values. Further details on the calculation of the plasma frequency can be found in Ref. 24.

Finally the optical constants, the refraction index, n , and the extinction coefficient, κ , and the absorption, A ,

reflection, R , and transmission, T , are calculated using the standard expressions:

$$n = \frac{1}{\sqrt{2}} \sqrt{\varepsilon^{(1)} + \sqrt{(\varepsilon^{(1)})^2 + (\varepsilon^{(2)})^2}} \quad (6)$$

$$\kappa = \frac{1}{\sqrt{2}} \sqrt{-\varepsilon^{(1)} + \sqrt{(\varepsilon^{(1)})^2 + (\varepsilon^{(2)})^2}} \quad (7)$$

$$A = 1 - \exp(-\kappa \omega d/c) \quad (8)$$

$$R = \frac{(n-1)^2 + \kappa^2}{(n+1)^2 + \kappa^2} \quad (9)$$

$$T = (1-R)(1-A), \quad (10)$$

with $\varepsilon^{(1)}$ and $\varepsilon^{(2)}$ the real and imaginary part of ε , d the slab thickness and c the speed of light in vacuum. The reflection and transmission spectra are constructed to simulate the substrate/ $\text{Mg}_x\text{Ti}_{(1-x)}\text{H}_2$ /palladium setup as was used in the experiments by Borsa *et al.*^{6,9} All internal reflections and absorptions in the three layer system are taken into account.

III. STRUCTURES

The calculation of the dielectric functions is performed using the crystal structures developed in Ref. 10. A brief summary of compositions and cell parameters is given in Table I. In short they were constructed in the following way.

In the case of $x = 0.875$ the simple cell is just the optimized experimental cell with composition $\text{Mg}_{28}\text{Ti}_4\text{H}_{64}$. For $x = 0.5$ and 0.75 , two and three atoms, respectively, out of the four titanium atoms in the conventional fcc TiH_2 cell were replaced by magnesium. Thus the unit cells have compositions $\text{Mg}_2\text{Ti}_2\text{H}_8$ and Mg_3TiH_8 respectively.

To simulate the random alloys super cells are used. These are also based on the fluorite Ti_4H_8 ($Z = 1$) building block. For $x = 0.5$ and 0.75 $2 \times 2 \times 2$ super cells were constructed and for $x = 0.875$ a $2 \times 1 \times 1$ super cell. Again Ti were replaced by Mg, but now such as to approximate random alloys most efficiently (see Ref. 10 for details).

For all the models constructed the positional and cell parameters were relaxed. The cells remain close to cubic, see Table I. The angles between the crystal axes are close to 90° , except for the $x = 0.75$ and 0.875 super cells where there is a small deviation.

IV. DIELECTRIC FUNCTIONS

A. Interband dielectric functions

Figures 2 and 3 show the calculated imaginary parts of the interband dielectric functions in the simple and super cells respectively. In general the dielectric functions exhibit a peak at low energy, below 2 eV, followed by a

TABLE I: Number of formula units (Z), lattice parameters (\AA) and shortest Ti-Ti interatomic distances (\AA). The first row for each composition contains the data of the simple cell and the second of the super cell.

x	Z	a	b	c	Ti-Ti
0.5	4	4.72	4.72	4.65	3.16
	32	9.08	9.03	9.09	3.15
0.75	4	4.62	4.62	4.62	4.62
	32	9.29	9.30	9.27	3.13
0.875	32	9.36	9.36	9.36	6.62
	64	18.75	9.42	9.73	3.08

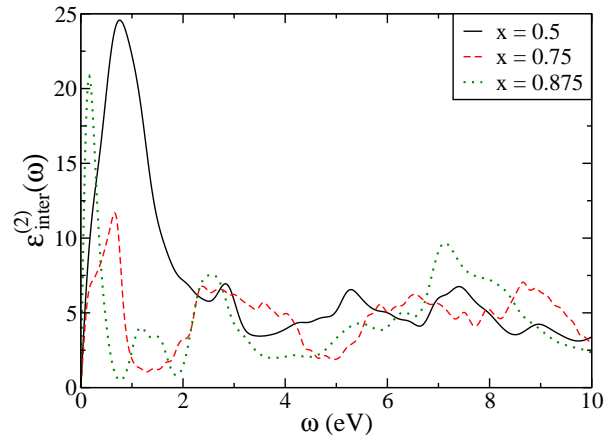


FIG. 2: (Color online) Imaginary parts of the interband dielectric functions of $\text{Mg}_x\text{Ti}_{(1-x)}\text{H}_2$ in the primitive cells.

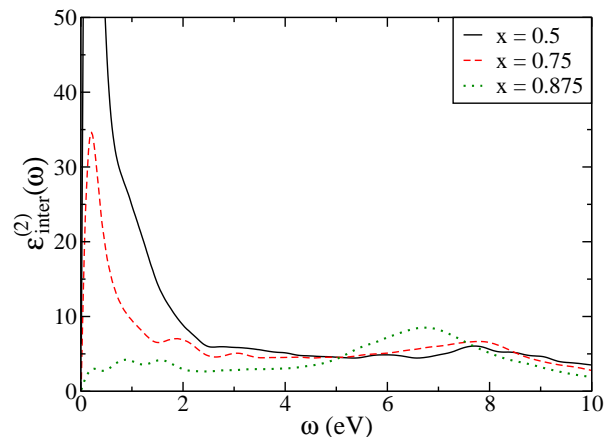


FIG. 3: (Color online) Imaginary parts of the interband dielectric functions of $\text{Mg}_x\text{Ti}_{(1-x)}\text{H}_2$ in the super cells. For $x = 0.5$ the dielectric function peaks to a value of 130.

relatively flat tail. In the super cells the dielectric functions have higher peaks and flatter tails. An exception is the dielectric function of the $x = 0.875$ super cell. It does not have a peak at low energy.

To understand the main features of the dielectric func-

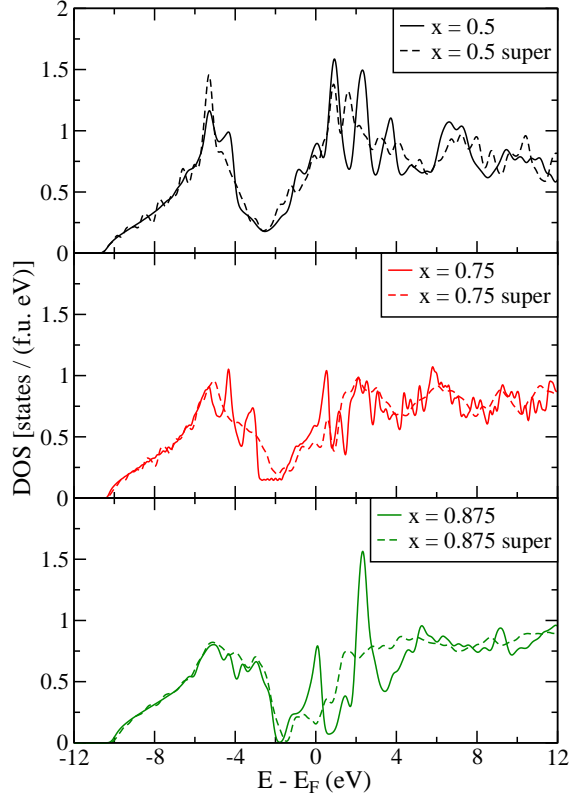


FIG. 4: (Color online) Electronic densities of state of the simple and super cells for the three compositions of $\text{Mg}_x\text{Ti}_{(1-x)}\text{H}_2$. The zero of energy is taken at the Fermi level.

tions we study the densities of states (DOS', Fig. 4). Below the Fermi level the DOS' have an approximately triangular shape with a predominant hydrogen- s and magnesium- s and p character. At the Fermi level the DOS' are dominated by titanium- d states. Above the Fermi level the DOS' have a mixed character of hydrogen- s and p , magnesium- s and p and titanium- d . As an illustration the angular momentum projected partial DOS' of the simple cell with $x = 0.75$ is shown in Fig. 5.

The electron density is localized at both the hydrogen and titanium atoms. This is illustrated in Figure 6, where the electron localization function (Ref. 25) is plotted, also for the simple cell $\text{Mg}_{0.75}\text{Ti}_{0.25}\text{H}_2$. At the titanium atoms the only available states are of d -character. Since $d-d$ transitions are very weak the main contribution to the dielectric function is from $s-p$ transitions on the hydrogen atoms.

In first order the imaginary part of the dielectric function can be described as the joint density of states (JDOS) divided by ω^2 . The hydrogen DOS has a dip near the Fermi energy. It increases when moving away from the Fermi energy, both to lower and higher energies. This causes the JDOS at the hydrogen atoms to increase more than linearly (in the region from 0 to about 8 eV). When

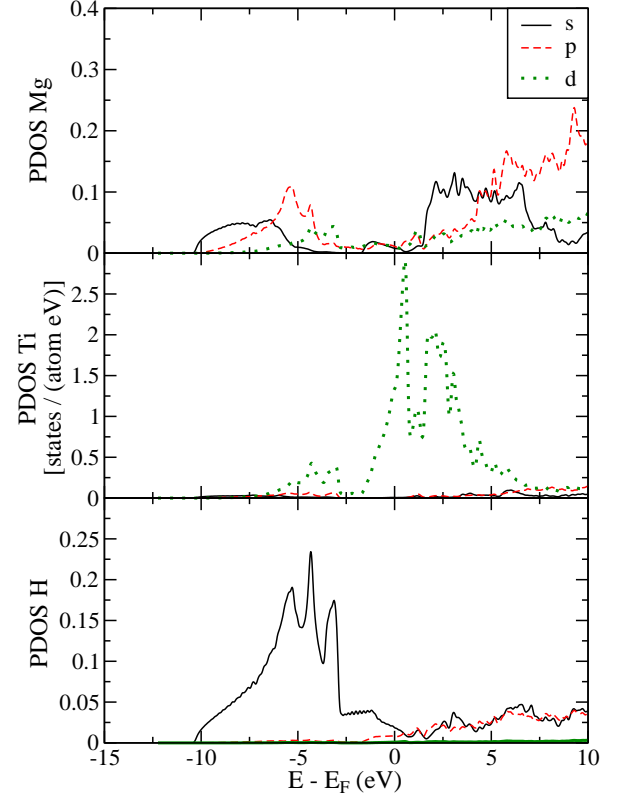


FIG. 5: (Color online) Angular momentum projected partial densities of states (PDOS) [states/(atom eV)] of $\text{Mg}_{0.75}\text{Ti}_{0.25}\text{H}_2$ in the simple unit cell. The zero of energy is at the Fermi level. The PDOS' are calculated in spheres with radii of 1.3, 1.3 and 0.8 Å for Mg, Ti and H respectively.

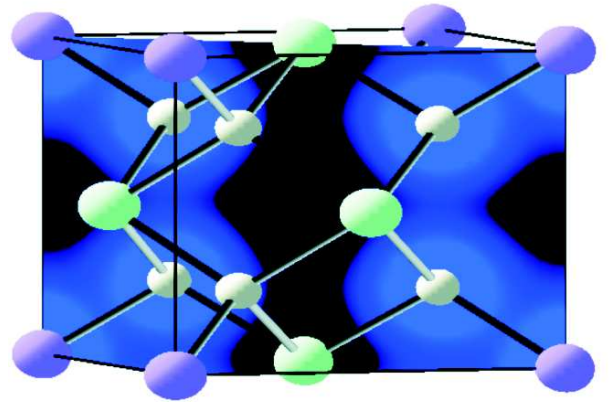


FIG. 6: (Color online) Electron localization function of $\text{Mg}_{0.75}\text{Ti}_{0.25}\text{H}_2$ in the simple unit cell. The Ti atoms are at the corners, the Mg atoms at the face centers and the H atom (small) are inside the cell. The electron localization function is plotted on a (110) cut-plane. Localization at the H and Ti atoms is evident.

TABLE II: Squared plasma frequencies, ω_p^2 (eV²), from intra-band transitions.

	simple cell	super cell
$x = 0.5$	10.7	1.3
$x = 0.75$	12.8	0.4
$x = 0.875$	8.6	0.1

divided by ω^2 this increase is rather effectively compensated. Hence the dielectric function does not vary much in the interval from 2 to 8 eV. This reasoning applies for all titanium concentrations that we considered. In the super cells the averaging over the various hydrogen DOS' gives rise to a further leveling out of the dielectric functions. Of course vibrational effects, that are lacking in our 0 K calculation, will even further smoothen the dielectric functions.

The peaks at the lower end of the energy range do arise from d-d transitions on the Ti atoms. Although their oscillator strength is small, division by ω^2 causes them to stand out nevertheless. For $x = 0.875$ the Ti DOS at E_{Fermi} is strongly suppressed in the super cell (see Fig. 4). This correlates with the absence of the peak in $\epsilon_{\text{inter}}^{(2)}$ for the super cell at this composition (Figs. 2, 3). At the other two compositions, we see no clear correlation between difference in DOS and peak shape (comparing simple and super cells). The higher peaks in the DOS in the super cells can be understood when we realize that the effective “back folding” of the d bands and their mutual interactions (caused by the randomization) results in a flattening of the bands. Some of these bands will be very close to E_{Fermi} and their transitions will thus be “boosted”, both by the flatness of the bands and the small transition energy. This discussion anticipates the discussion in the next section.

B. Intraband plasma frequencies

The intraband plasma frequencies, which have been calculated according to Equation 5, are listed in Table II. The squared plasma frequencies from the super cell calculations are between one and two orders of magnitude smaller than those of the simple cells. Therefore the edge on the free carrier reflectivity occurs at considerably lower energies in the random alloys. In our models the maximum ω_p is 1.1 eV. This is, however, for only one realization of a random model at $x = 0.5$ and it is well conceivable that calculations on large models could yield even lower ω_p . For the simple cells, the plasma frequencies are approximately 3 eV, hence these systems are highly reflecting for $\omega < 3$ eV.

Eq. 5 is a good starting point for a discussion of the trends across Table II. It basically states that the squared plasma frequency is proportional to the product of the electron density and the square of the slope of the energy bands, both calculated at the Fermi level. In the

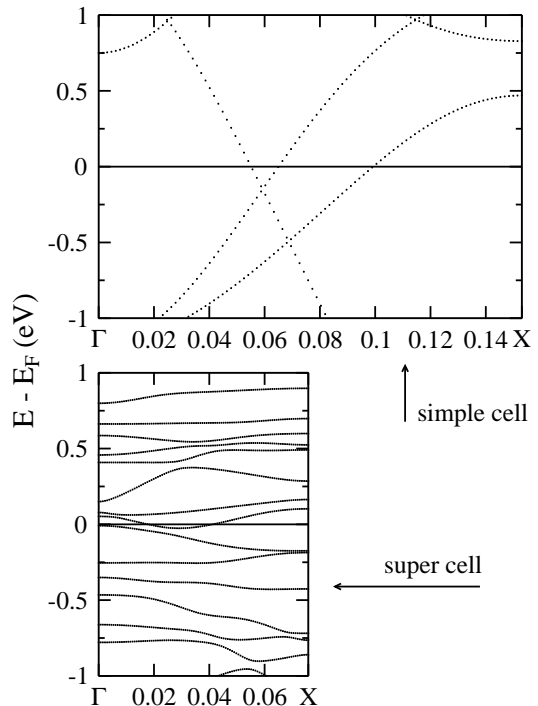


FIG. 7: Electronic energy band structure of $\text{Mg}_{0.75}\text{Ti}_{0.25}\text{H}_2$ in the simple and super cell along the Γ -X direction.

super cells ω_p^2 clearly follows the density of states (see, Fig. 4) as a lower concentration of titanium means a lower amount of free electrons. In the simple cells this trend is not obvious. Subtle changes in the shape of the DOS, i.e. bandstructure effects, make for less changes in the electron density at the Fermi level. Consistently the plasma frequency shows little variation. This, however, does not imply that small changes in the slope of the energy bands do not play an equally important role here.

The difference between the simple and super cells of the same composition is explained by a decrease in energy band slope. The DOS' at the Fermi level are of comparable size, at least for compositions with $x = 0.5$ and $x = 0.75$. This clearly points to the change in $\partial\epsilon_{n\mathbf{k}}/\partial\epsilon_{\mathbf{k}}$ as the cause of the significant decrease of ω_p . This is corroborated by inspection of the band structure, that is plotted in Fig. 7 for $\text{Mg}_{0.75}\text{Ti}_{0.25}\text{H}_2$ for both the simple and super cell. We see that the bandstructure of the supercell cannot be understood as a simple back-folding of the bands. The randomness in the structure has induced many interactions between the d-bands, leading to a dramatic reduction of their slopes. Going to even larger super cells, the effect may become even stronger, and the free carrier reflection concomitantly reduced. Such a calculation goes beyond the present study. It may require a different formalism as the reciprocal space description of Eq. 5 is bound to break down for truly random systems.

Interestingly, the flatness of the energy bands also

makes that the effective mass of the “free” electrons is rather high. This goes some way to explain the rather high resistivity measured for these systems. The “flat bands” also point to a possible localization of carriers.

For $x = 0.875$ the reduction of ω_p^2 cannot be understood as a reduction of only $\partial\epsilon_{nk}/\partial\mathbf{k}$. From Fig. 4 a substantial reduction of the DOS at E_{Fermi} is evident. Hence reduction of ω_p^2 is much stronger than for $x = 0.5$ and $x = 0.75$.

To obtain the dielectric functions of the materials we just add the interband part of Sect. IV A and intraband parts obtained from ω_p according to Eq. 1. It was already noted above that the impact on the reflection in the visible range will be substantial for the simple cells. The values of ω_p^2 in the super cells are low enough to only induce minor corrections to the interband dielectric function. The implications of the corrections will be discussed in the next Section.

V. DISCUSSION

The calculations on the random alloy super cells clearly demonstrate that breaking of the short range order results in two important effects: (a) The interband dielectric function is smoothened and (b) the plasma frequency is lowered. The first translates in smoother reflection and transmission spectra for the super cells. The second results in a lower reflection edge. The simple cells have almost full reflection up to 1–2 eV whereas in the super cells full reflection only occurs below ~ 0.3 eV.

Figure 8 shows the calculated reflection and transmission of a film simulating closely the experimental setup as used by Borsa *et al.*⁹ The simulated film consists of 10 nm Paladium / 200 nm $\text{Mg}_x\text{Ti}_{(1-x)}\text{H}_2$ / ($k = 0$) quartz substrate layers, where we use the $\epsilon(\omega)$ calculated in the super cells for the $\text{Mg}_x\text{Ti}_{(1-x)}\text{H}_2$ layer. The plotted range is that of a Perkin Elmer Lambda 900 diffraction spectrometer. For comparison; visible light lies in the range of 1.65–3.26 eV. The general features and trends as a function of Ti content in both reflection and transmission are in agreement with the trends observed in the experiments.⁹ Indeed the reflection is low and our calculations describe a “black state”. With decreasing Ti content the reflection decreases and the transmission increases.

Since experiments were performed on magnesium/titanium ratios $x = 0.7, 0.8$, and 0.9 , that would have required very large super cells, a detailed comparison can only be made partially. Interpolating between the experimental values for 0.7 and 0.8 we can make a reasonable comparison with the calculated results for $x = 0.75$. The experimental reflection lies about 5 %Pt. lower than the calculated one but the shape of the curve is very similar. The experimental transmission drops from 6.5%–0% in the range from 0.5–3 eV, it hence lies about a factor 3 higher than the calculated one. The shapes of the transmission curves, however shows good

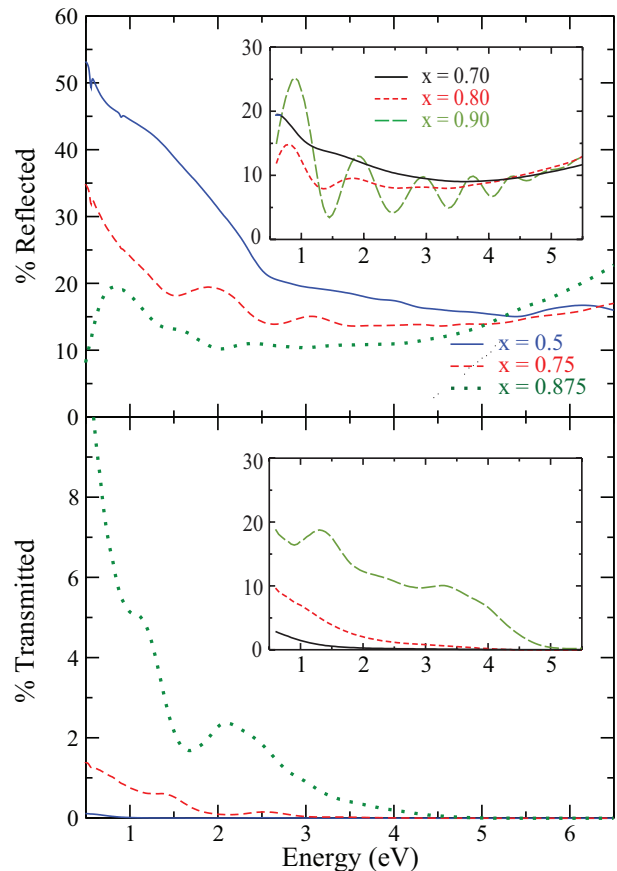


FIG. 8: (Color online) Reflection and transmission of a 10 nm Paladium / 200 nm $\text{Mg}_x\text{Ti}_{(1-x)}\text{H}_2$ / ($k = 0$) quartz substrate film. For the dielectric function of $\text{Mg}_x\text{Ti}_{(1-x)}\text{H}_2$ the results for the supercell, including inter and intraband contributions, are used. The inset shows experimental results from Ref. 9, reproduced with permission, copyright American Physical Society (2007).

agreement.

Comparing the calculated values for $x = 0.875$ to the experimental results for $x = 0.9$ we again see somewhat lower values for the experimental reflection. Furthermore, the slight oscillation seen in the calculated spectrum, caused by interference, is much stronger in the experimental spectrum. The main difference in the transmission lies in the energy range below 1 eV where the calculated transmission is much larger than the experimental values. This difference could point to an underestimation of the ω_p^2 in the super cell $x = 0.875$ calculation.

From the correspondence between the experimental and calculated optical spectra we conclude that the “black state” can already be explained from moderate-size randomized super cells. Put into other words: randomized models containing only 32 to 64 formula units allow for a breaking of the order on a length-scale such as to lower the reflection edge and smoothen the spectra. This does not necessarily imply that a randomization at larger length scales, with a concomitant increase of the

short range order, e.g. in the coherent crystal picture proposed by Borsa *et al.*⁹, would be inconsistent with experiment. Indeed, the coherent crystal model is supported by various observations, e.g. the large positive enthalpy of mixing of Ti and Mg. Moreover, for $x = 0.875$ our modeling seems to underestimate ω_p , suggesting that the short range disorder may have disrupted the band dispersion too much. A full first-principles study of necessarily larger models with more short range order is beyond present computational capabilities. Such a study is desirable. However, with the present randomized models we can capture most of the essential physics of $\text{Mg}_x\text{Ti}_{1-x}\text{H}_2$.

Acknowledgments

The authors thank Prof. G. Kresse and J. Harl (Universität Wien) for the use of the optical packages and R. Gremaud (Vrije Universiteit) for running the reflection/transmission simulations. This work is part of the Sustainable Hydrogen Programme of the Advanced Catalytic Technologies for Sustainability (ACTS) and the Stichting voor Fundamenteel Onderzoek der Materie (FOM), both financially supported by the Nederlandse Organisatie voor Wetenschappelijk Onderzoek (NWO).

-
- ¹ J. N. Huiberts, R. Griessen, J. H. Rector, R. J. Wijnaarden, J. P. Dekker, D. G. de Groot, and N. J. Koeman, *Nature* **380**, 231 (1996).
 - ² P. van der Sluis, M. Ouwerkerk, and P. A. Duine, *Appl. Phys. Lett.* **70**, 3356 (1997).
 - ³ T. J. Richardson, J. L. Slack, R. D. Armitage, R. Kostecki, B. Farangis, and M. D. Rubin, *Appl. Phys. Lett.* **78**, 3047 (2001).
 - ⁴ J. Isidorsson, I. A. M. E. Giebels, R. Griessen, and M. Di Vece, *Appl. Phys. Lett.* **80**, 2305 (2002).
 - ⁵ W. Lohstroh, R. J. Westerwaal, B. Noheda, S. Enache, I. A. M. E. Giebels, B. Dam, and R. Griessen, *Phys. Rev. Lett.* **93**, 197404 (2004).
 - ⁶ D. M. Borsa, A. Baldi, M. Pasturel, H. Schreuders, B. Dam, R. Griessen, P. Vermeulen, and P. H. L. Notten, *Appl. Phys. Lett.* **88**, 241910 (2006).
 - ⁷ W. Lohstroh, R. J. Westerwaal, J. L. M. van Mechelen, H. Schreuders, B. Dam, and R. Griessen, *J. Alloy. Compd.* **430**, 13 (2007).
 - ⁸ M. Slaman, B. Dam, M. Pasturel, D. M. Borsa, H. Schreuders, J. H. Rector, and R. Griessen, *Sens. Actuator B-Chem.* **123**, 538 (2007).
 - ⁹ D. M. Borsa, R. Gremaud, A. Baldi, H. Schreuders, J. H. Rector, B. Kooi, P. Vermeulen, P. H. L. Notten, B. Dam, and R. Griessen, *Phys. Rev. B* **75**, 205408 (2007).
 - ¹⁰ S. Er, M. J. van Setten, G. A. de Wijs, and G. Brocks, in preparation (2007).
 - ¹¹ D. Kyo, T. Sato, E. Ronnebro, N. Kitamura, A. Ueda, M. Ito, S. Katsuyama, S. Hara, D. Noreus, and T. Sakai, *J. Alloy. Compd.* **372**, 213 (2004).
 - ¹² R. A. H. Niessen and P. H. L. Notten, *Electrochem. Solid State Lett.* **8**, A534 (2005).
 - ¹³ P. Vermeulen, R. A. H. Niessen, D. M. Borsa, B. Dam, R. Griessen, and P. H. L. Notten, *Electrochem. Solid State Lett.* **9**, A520 (2006).
 - ¹⁴ P. Vermeulen, R. A. H. Niessen, and P. H. L. Notten, *Electrochem. Commun.* **8**, 27 (2006).
 - ¹⁵ G. Kresse and J. Furthmüller, *Phys. Rev. B* **54**, 11169 (1996).
 - ¹⁶ G. Kresse and J. Furthmüller, *Comput. Mater. Sci.* **6**, 15 (1996).
 - ¹⁷ G. Kresse and J. Hafner, *Phys. Rev. B* **47**, 558 (1993).
 - ¹⁸ G. Kresse and D. Joubert, *Phys. Rev. B* **59**, 1758 (1999).
 - ¹⁹ P. E. Blochl, *Phys. Rev. B* **50**, 17953 (1994).
 - ²⁰ J. P. Perdew, J. A. Chevary, S. H. Vosko, K. A. Jackson, M. R. Pederson, D. J. Singh, and C. Fiolhais, *Phys. Rev. B* **46**, 6671 (1992).
 - ²¹ S. G. Louie, S. Froyen, and M. L. Cohen, *Phys. Rev. B* **26**, 1738 (1982).
 - ²² P. E. Blochl, O. Jepsen, and O. K. Andersen, *Phys. Rev. B* **49**, 16223 (1994).
 - ²³ M. Gajdoš, K. Hummer, G. Kresse, J. Furthmüller, and F. Bechstedt, *Phys. Rev. B* **73**, 045112 (2006).
 - ²⁴ J. Harl, G. Kresse, L. D. Sun, M. Hohage, and P. Zeppenfeld, *Phys. Rev. B* **76**, 035436 (2007).
 - ²⁵ B. Silvi and A. Savin, *Nature* **371**, 683 (1994).